

# Negative Differential Resistance of Oligo(Phenylene Ethynylene) Self-Assembled Monolayer Systems: The Electric-Field-Induced Conformational Change Mechanism

Hyunjun Kim,<sup>†,‡</sup> Seung Soon Jang,<sup>§</sup> Richard A. Kiehl,<sup>||</sup> and William A. Goddard<sup>†,‡,\*</sup>

<sup>†</sup>Graduate School of EEWS (WCU), Korea Advanced Institute of Science and Technology, Daejeon 305-701, Republic of Korea

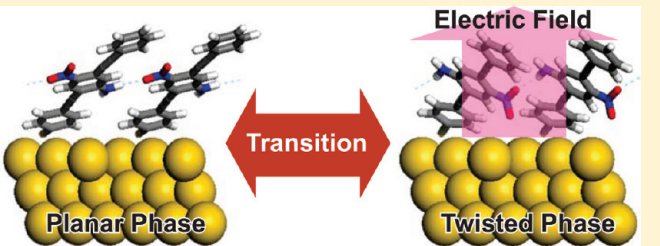
<sup>‡</sup>Materials and Process Simulation Center, California Institute of Technology, Pasadena, California 91125, United States

<sup>§</sup>School of Materials Science and Engineering, Georgia Institute of Technology, Atlanta, Georgia 30332-0245, United States

<sup>||</sup>Department of Electrical and Computer Engineering, University of California, Davis, California 95616, United States

Supporting Information

**ABSTRACT:** We investigate here a possible mechanism for the room temperature negative differential resistance (NDR) in the Au/AN-OPE/RS/Hg self-assembled monolayer (SAM) system, where AN-OPE = 2'-amino,5'-nitro-oligo(phenylene ethynylene) and RS is a C<sub>14</sub> alkyl thiolate. Kiehl and co-workers showed that this molecular system leads to NDR with hysteresis and sweep-rate-dependent position and amplitude in the NDR peak. To investigate a molecular basis for this interesting behavior, we combine first-principles quantum mechanics (QM) and mesoscale lattice Monte Carlo methods to simulate the switching as a function of voltage and voltage rate, leading to results consistent with experimental observations. This simulation shows how the structural changes at the microscopic level lead to the NDR and sweep-rate-dependent macroscopic *I*–*V* curve observed experimentally, suggesting a microscopic model that might aid in designing improved NDR systems.



## INTRODUCTION

Esaki's discovery of the negative differential resistance (NDR) in Ge p–n diodes opened a new phase in semiconductor devices.<sup>1</sup> NDR devices could enable faster and more efficient circuits by reducing the number of transistors required; hence, they also have many potential applications such as high-speed integrated circuits and low-power memories. As the scale of electronic devices is reduced toward nanoscale sizes, it will be useful to realize NDR in molecular electronic systems.<sup>2–13</sup>

Derivatives of oligo(phenylene ethynylene) (OPE) have been identified as possible candidates for the molecular junctions due to their rigidity and highly conducting (fully conjugated) characteristics.<sup>5,11–19</sup> Chen et al. reported that a self-assembled monolayer (SAM) of amino-nitro-substituted OPE (AN-OPE) between two Au electrodes exhibits NDR at 60 K with an applied voltage of ~2 V. The current–voltage (*I*–*V*) curve is fully reversible, but the NDR peak decays as the temperature increases. This NDR has been rationalized by an electrochemical oxidation/reduction or resonant-tunneling mechanism.<sup>15–17</sup> Support for this oxidation/reduction mechanism was provided by the correspondence between the threshold potential for the electrical conductance (2.09 V) and the electrochemical potential (1.67 V).<sup>15,19</sup> However, the resonant-tunneling cannot explain the hysteretic NDR.<sup>8</sup>

Devices showing NDR at room temperature (RT) are of interest for many practical applications.<sup>20,21</sup> However, the poor reproducibility in device construction and the limited device stability have hampered extensive study on NDR. Kiehl and co-workers showed that a SAM of AN-OPE deposited on an Au electrode coupled to a Hg electrode covered with a tetradecane-thiolate (RS) leads to a more well-defined and stable NDR at RT.<sup>5</sup> In this system, a distinct sweep-rate dependence in the NDR hysteresis loop was observed for a bias voltage near ~0.6 V. The presence of hysteresis rules out a resonant tunneling mechanism.<sup>3,4,8–10</sup> Based on the observed hysteresis and a variety of detailed features of the characteristics, Kiehl et al. proposed a charge capture (QC) mechanism to explain the macroscopic *I*–*V* behavior. However, an atomistic level analysis of such a charge capture process and other possible mechanisms has not yet been established.

Several studies suggest that the conformational change would be a plausible mechanism to explain hysteretic *I*–*V* curve,<sup>14,22</sup> and the external electric field can induce conformational change of the molecule in the junction.<sup>14,23–26</sup> In particular, Donhauser et al. reported STM studies in which isolated AN-OPE molecules

Received: December 2, 2010

Revised: January 4, 2011

Published: February 16, 2011

contained in a dodecane-thiolate SAM on an Au substrate show at least two states having different conductances.<sup>14</sup> They showed that the transition from the high-conductance state to the low-conductance state is switched by applying an external electric field. However, no detailed atomic level description of the mechanism was provided.

In this paper, we use first-principles theory to analyze the sweep-rate-dependent hysteresis of NDR observed in Kiehl's system, focusing on the possibility of electric-field-based conformational changes. We find that this system has two states:

- high-conductance phase stable at low fields and
- low-conductance phase stable high-fields.

The transition between the two phases is driven by the interaction between the external field and the molecular dipole moment of the middle benzene ring in AN-OPE. Using Monte Carlo simulations with coarse-grained Hamiltonian, we investigated how such a molecular conformational change results in a sweep-rate-dependent hysteresis in the NDR as well as the detailed kinetics of transition.

## RESULTS AND DISCUSSION

**Two Conformations of AN-OPE.** We first investigated the conformations of AN-OPE molecules when they are packed on top of Au surface. To obtain the structures and energetics of AN-OPE SAM, we carried out density functional theory (DFT) calculations using the Vienna Ab Initio Simulation Package (VASP).<sup>27</sup> We employed the Perdew–Burke–Ernzerhof (PBE) generalized gradient approximation exchange-correlation density functional with a plane wave basis set (540 eV cutoff), and only the gamma point is sampled in the reciprocal space for the evaluation of relative energetics and structures of these large systems (67 atoms per periodic cell).

The Au electrode part is modeled as a three-layer Au(111) surface with all gold atoms fixed at their bulk value ( $a = 2.8838 \text{ \AA}$ ). Then, the AN-OPE molecules were anchored on the  $3 \times 3$  Au(111) surface through sulfur atoms with hexagonal packing.

Figure 1a shows the optimized conformation of AN-OPE SAM. The three phenyl rings are coplanar, forming a well-conjugated structure, which we label as P (for planar). Here the lowest ring is connected to the Au electrode via a thiolate group. The middle ring (containing the functional groups) has a twist angle of  $\chi = 4^\circ$  with respect to the bottom ring ( $\chi = 0^\circ$  for the isolated OPE). This structure packs on the Au surface as  $(3 \times 3)$ , with the axis of the molecule along the  $[1\bar{1}00]$  direction, and a tilt angle  $\theta = 66^\circ$  from the  $z$ -axis. Interestingly, we found that the adjacent amino and nitro groups form hydrogen bonding (HB) networks along the  $[11\bar{2}0]$  direction.

To understand the local electronic structure and local interactions of the organic molecular part, we performed a single-point nonperiodic QM calculation of an isolated AN-OPE molecule with three Au atoms that are connected to the AN-OPE. Here, we utilized the Jaguar package<sup>28</sup> with same PBE exchange-correlation functional and LACVP\*\* basis set.

We found that the polar amino and nitro groups lead to a large dipole moment of 9.24 (7.22) debye (D) with the  $z$ -axis component ([0001] direction) of 5.74 (3.55) D, the component along  $[1\bar{1}00]$  (tilt direction) of 4.44 (3.35) D, and the component along  $[11\bar{2}0]$  (HB direction) of 5.72 (5.32) D. These dipole moments were determined from the analysis of Mulliken charges, while the values in parentheses are from the full quantum mechanical wave functions.

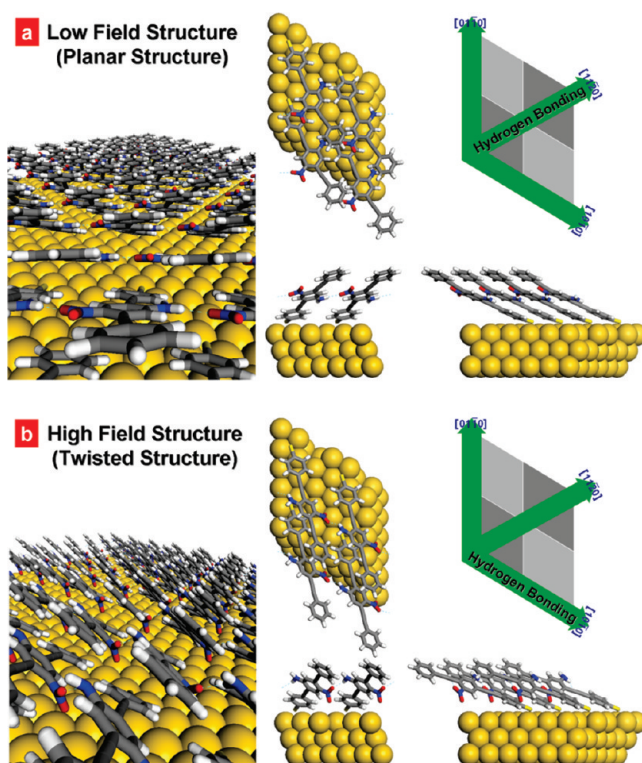


**Figure 1.** (a) Optimized geometry for the low-field structure (P) of AN-OPE SAM. Here [0001] is the surface normal, and the views are along the  $z$ -axis (upper middle),  $y$ -axis (lower middle), and  $x$ -axis (lower right). The left picture is a perspective along the axis of one plane of molecules. The hydrogen bonding network is aligned along the  $[11\bar{2}0]$  direction. (b) Optimized geometry for the high-field structure (T) of AN-OPE SAM. Here [0001] is the surface normal, and the views are along the  $z$ -axis (upper middle),  $y$ -axis (lower middle), and  $x$ -axis (lower right). The left picture is a perspective along the axis of one plane of molecules. The hydrogen bonding network is aligned along the  $[10\bar{1}0]$  direction.

**Table 1.** AN-OPE Interaction Energies  $U_{ij}$  for MC Calculations<sup>a</sup>

	$[10\bar{1}0]$ pair	$[01\bar{1}0]$ pair	$[11\bar{2}0]$ pair
$\{i, j\} \subset P$	−3.95	−5.00	−7.19
$\{i, j\} \subset T$	−7.66	−3.12	−0.61
$\{i \in P, j \in T\} \text{ or } \{i \in P, j \in P\}$	−5.70	−2.56	3.13

<sup>a</sup>All energy values are in kcal/mol.

The inter AN-OPE interaction energies on the SAM,  $U_{ij}$ , are determined from the difference between dimer energy and doubled monomer energy (defined in eq 1) when two isolated AN-OPE molecules are aligned along three different directions of  $[10\bar{1}0]$ ,  $[01\bar{1}0]$ , and  $[11\bar{2}0]$ :

$$U_{ij} = E_{2(\text{AN-OPE} + 3\text{AU})} - 2 \times E_{\text{AN-OPE} + 3\text{AU}} \quad (1)$$

The value of  $U_{ij}$  between two planar conformations is shown in Table 1. We note that  $U_{ij}$  along the  $[11\bar{2}0]$  direction shows the largest stabilization energy of −7.19 kcal/mol, which results from the HB interactions.

We obtained another conformation named T (for twisted) in which the AN-OPE molecule is tilted along  $[1\bar{1}00]$ . Figure 1b shows the T conformation, which is 4.85 kcal/mol less stable

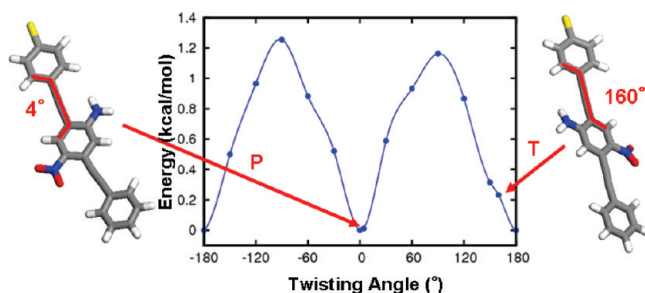


**Figure 2.** Torsional strain energy  $E_i^{\text{torsion}}$  as a function of twisting angle  $\chi$  from QM (PBE) on the isolated molecule. The energy at  $\chi = 4^\circ$  (corresponding to P) is 0.01 kcal/mol higher than the ground state energy at  $\chi = 0^\circ$ . The energy at  $\chi = 160^\circ$  (which corresponds to T) is 0.23 kcal/mol higher than the energy at  $\chi = 0^\circ$ , leading to the 0.22 kcal/mol higher  $E_i^{\text{torsion}}$  of T compared to  $E_i^{\text{torsion}}$  of P.

than P. The middle and terminal phenyl rings are rotated from the bottom one by  $\chi = 160^\circ$ . Although this twist angle is not stable for the isolated AN-OPE, it becomes metastable in the packed system (Figure 2). The rotation of the middle ring changes the direction of amino/nitro groups along  $[10\bar{1}0]$  from  $[11\bar{2}0]$ , leading the hydrogen bond network to be aligned along  $[10\bar{1}0]$ . The axis of the molecule is at  $\theta = 71^\circ$  from the z-axis.

From QM calculations, we find that the dipole moment of T is 8.71 (6.88) D with the component along  $[0001]$  of 7.04 (4.62) D, a component along  $[1\bar{1}00]$  (tilt direction) of  $-3.32$  ( $-3.40$ ) D, and a component along  $[\bar{1}010]$  (HB direction) of 5.12 (5.10) D.

Using eq 1, the values of  $U_{ij}$  between two isolated T conformation AN-OPEs are determined and shown in Table 1. For the T conformation,  $U_{ij}$  along the  $[\bar{1}010]$  direction (HB network direction) is the most stable with the value of  $-7.66$  kcal/mol.

**Electrical Conductivities of P and T.** Based on the calculated geometries of the ground state (P) and the metastable state (T) phase of AN-OPE SAM, we estimated the electrical conductivities ( $\sigma$ ) of both SAM conformations. Current–voltage ( $I$ –V) performance through the device is estimated by combining Green's function theory with the DFT Hamiltonian. Since this functionality is implemented in the SeqQuest program,<sup>29,30</sup> we determined the DFT Hamiltonian for transmittance calculations using the SeqQuest program with same PBE functional. These calculations partition the tunneling Hamiltonian using the Gaussian basis function representation. The current is calculated using eq 2

$$I(V) = \frac{2e}{h} \int_{-\infty}^{\infty} T(E, V) [f_1(E, V) - f_2(E, V)] dE \quad (2)$$

where  $T(E, V)$  is the transmission function of the AN-OPE SAM part.

The experiments use a top Hg electrode covered with a tetradecane-thiolate (RS), the atomic structure of which is not certain due to the amorphous character of the Hg electrode and the fluctuations in the alkyl thiol at room temperature. Instead, our calculations use a second three-layer Au(111) surface 12 Å above the bottom electrode from the bottom Au(111) electrode, which is in contact with the AN-OPE SAM.

The density of states (DOS) and the transmission function  $T(E, V)$  of P and T phases are shown in Figure 3a and 3b, respectively. These were employed to obtain the  $I$ –V curve and  $\sigma$ –V curve (the derivative of the  $I$ –V curve) shown in Figure 4. Over the range of 0–1.5 V, we see that  $\sigma_P$  is  $\sim 10$  times larger than  $\sigma_T$  on average. To validate the effect of using an arbitrary

chosen position of top electrode, we placed the top electrode distant from the OPE SAM, which is 20 Å above the bottom electrode (see Figures S1 and S2). Due to the vacuum part introduced between two electrodes, the total tunneling current is dramatically decreased; however, the general tendency is similar. In particular, the key finding that the  $\sigma_P$  is larger than  $\sigma_T$  is observed regardless of the top electrode position, which can be understood as a consequence of more overlapped  $\pi$  orbitals of P conformation that can be used a current tunneling channel.<sup>33</sup>

**Coarse-Grained NN Interacting Hamiltonian.** To understand the kinetics of AN-OPE SAM during the voltage sweep, we first designed the nearest neighbor (NN) interacting Hamiltonian

$$H = \sum_{i=1}^N (E_i^{\text{torsion}} - D_i F) + \sum_{\text{NN}} U_{ij} \quad (3)$$

where  $E_i^{\text{torsion}}$  is the internal torsional energy of the  $i$ th AN-OPE molecule due to twisting the AN-OPE by an angle  $\chi$ . This is estimated from the energy versus twisting angle  $\chi$  curve (Figure 2), leading to 0.01 kcal/mol per AN-OPE when  $i \in P$  and 0.23 kcal/mol when  $i \in T$ .

$U_{ij}$  is the intermolecular interaction energy between  $i$ th and  $j$ th AN-OPE, where the summation over NN denotes that the summation is over nearest neighbors. There are two interactions each for three directions:  $[10\bar{1}0]$ ,  $[01\bar{1}0]$ , and  $[11\bar{2}0]$ . To avoid double counting, however, we used just one interaction per direction,  $U_{ij}$ . From the nonperiodic QM calculations, the  $U_{ij}$  terms when two AN-OPE molecules are in the same conformation, i.e.,  $\{i, j\} \subset P$  or  $\{i, j\} \subset T$ , were already determined and tabulated in Table 1. In order to obtain the rest of the terms, which are  $U_{ij}$  values when  $\{i \in P, j \in T\}$  or  $\{i \in T, j \in P\}$ , we performed molecular mechanics (MM) calculations because investigation of these terms requires at least a  $2 \times 2$  extended cell containing four AN-OPE molecules, which is a large cell to be examined by QM methods. We used the DREIDING force field<sup>31</sup> (FF) with the charges based on Mulliken charge analysis from Jaguar calculations. We considered seven possible packings within a  $2 \times 2$  unit cell:

- AP, all P's;
- AT, all T's;
- P3T1, 3 P's and 1 T;
- P2T<sub>10̄10</sub>, 2 P's and 2 T's aligned along  $[10\bar{1}0]$ ;
- P2T<sub>01̄10</sub>, 2 P's and 2 T's aligned along  $[01\bar{1}0]$ ;
- P2T<sub>11̄20</sub>, 2 P's and 2 T's aligned along  $[11\bar{2}0]$ ;
- P1T3, 1 P and 3 T's.

The relative energy of AT compared to AP is 4.97 kcal/mol from FF energy in agreement with the QM energy value of 4.85 kcal/mol, which ensures the quality of calculated FF energies. This good correspondence is because the inter-AN-OPE interactions are dominated by the van der Waal's energy and the electrostatic energy, which are unambiguously defined in FF parameters. Using these FF energies, we fitted the  $U_{ij}$  terms when  $\{i \in P, j \in T\}$  or  $\{i \in T, j \in P\}$  with a least-squared fitting method. The final values are shown in Table 1.

$D_i$  is the  $[0001]$  component ( $z$ -direction) of the dipole moment of the  $i$ th AN-OPE, and  $F$  is the  $[0001]$  component of the external electric field. To evaluate this term, we applied the electric field to the above seven different  $2 \times 2$  packed systems and then obtained the FF energies under external electric field of 1.2 V/Å. The fitted values based on these FF energies are  $D_i = 5.48$  D per AN-OPE when  $i \in P$  and 7.30 D when  $i \in T$ , which are quite comparable to

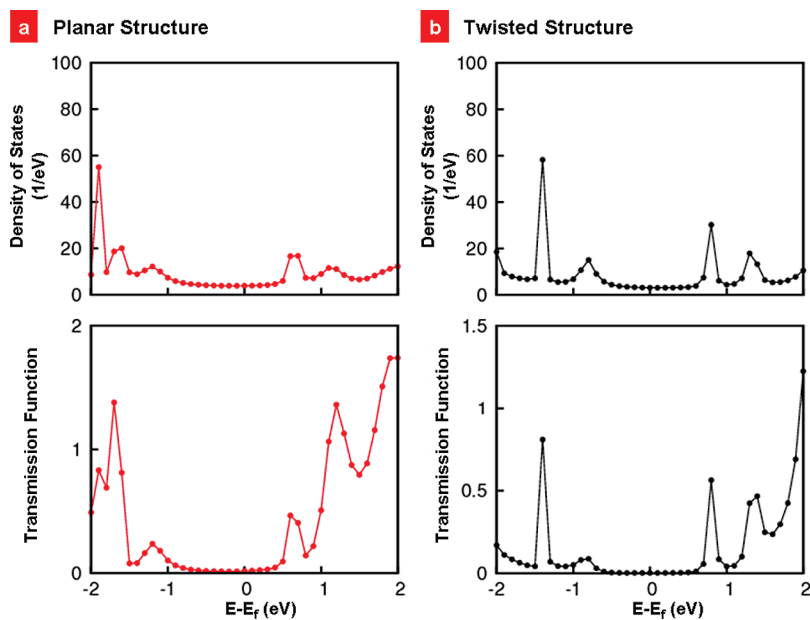


**Figure 3.** Density of states (DOS) and transmission function  $T(E)$  from QM calculations of (a) P structure and (b) T structure. The top electrode is located 12 Å above the bottom electrode.

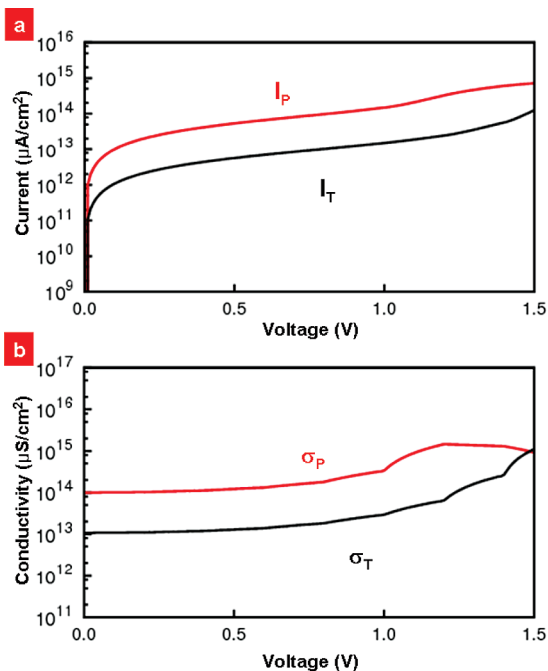


**Figure 4.** (a) Current through P conformation,  $I_P$ , and current through T conformation,  $I_T$ , versus the bias voltage  $V$  determined from the NEGF QM calculations using the DOS and  $T(E)$  of Figure S4. (b) Conductivity of P conformation,  $\sigma_P$ , and conductivity of T conformation,  $\sigma_T$ , versus the bias voltage  $V$  determined from (a). The top electrode is located 12 Å above the bottom electrode.  $\sigma_P$  is  $\sim 10$  times larger than  $\sigma_T$ .

the dipoles from Mulliken charge analysis, which are 5.74 and 7.03 D, respectively.

Final results from various methods, QM, FF, and NN models, are compared in Figure 5 without an external electric field (part b) and under 1.2 V/Å external electric field (part a). All relative energy values show good agreement with each other.

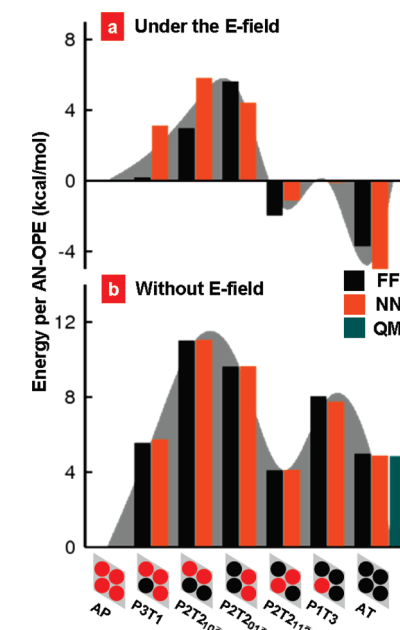


**Figure 5.** (a) Energies of various conformations of AN-OPE relative to the AP conformation computed with a 1.2 V/Å external field from FF calculations (black histograms) and NN model calculations (orange histograms). (b) Energies of various conformations of AN-OPE relative to the AP conformation computed with no external field from FF calculations (black histograms), NN model calculations (orange histograms), and QM calculations (green histograms).

**Response to Constant External Field.** To describe the dynamics and kinetics of a large simulation cell mimicking an AN-OPE SAM system, we performed a lattice Monte Carlo (MC) simulation using a simplified nearest neighbor (NN) interaction Hamiltonian (eq 3). This coarse-grained Hamiltonian is modeled from the first-principles methods.

We considered a two-dimensional rhombic MC simulation cell containing  $50 \times 50$  lattice points with periodic boundary

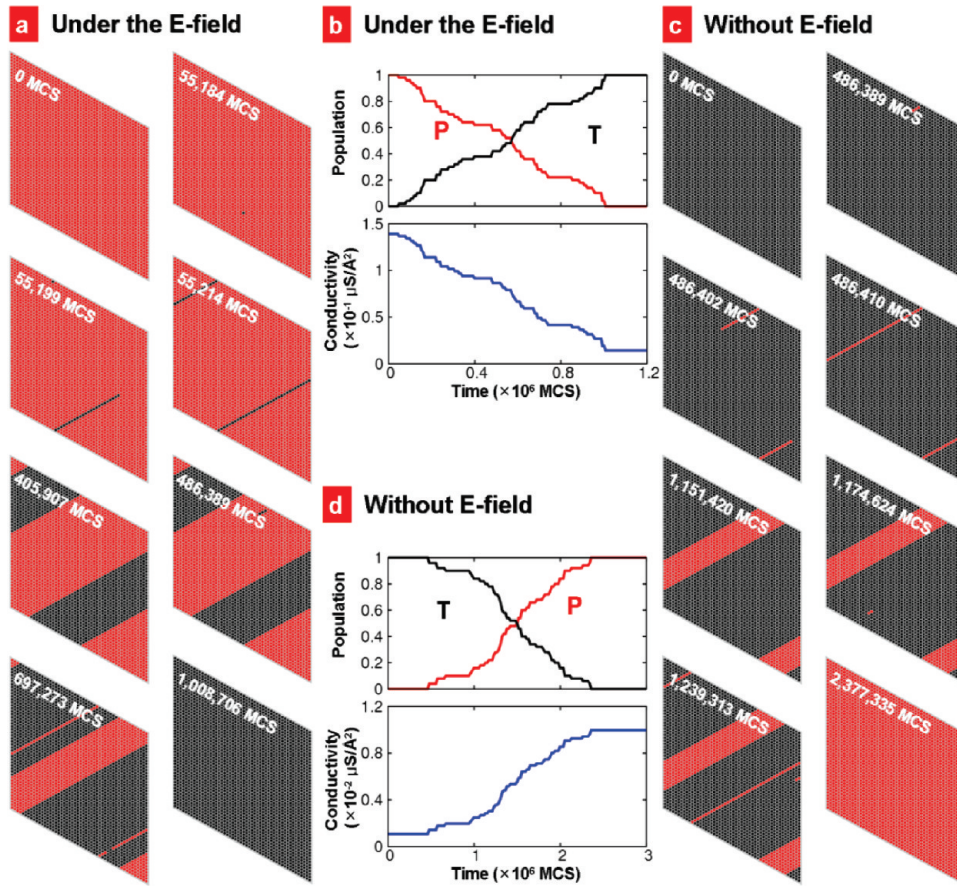


**Figure 6.** (a) Snapshots during P-to-T transition from MC simulation with  $1.2 \text{ V}/\text{\AA}$  external field. The first nucleation occurred at 55 184 MCS, then the line propagated until 55 214 MCS, and then the  $[1\bar{1}\bar{2}0]$  line propagated until 55 214 MCS. More nucleation and propagation along  $[1\bar{1}\bar{2}0]$  take place, and finally, the full system is transformed by 1 008 706 MCS. We note that increased bias voltage yields a faster P-to-T transition. (b) Time dependence of P and T populations and electrical conductivity through the SAM during P-to-T transition. (c) Snapshots during T-to-P transition from MC simulation without an external field. The first nucleation occurred at 486 389 MCS, and then the  $[1\bar{1}\bar{2}0]$  line propagates until 486 410 MCS. More nucleation and propagation along  $[1\bar{1}\bar{2}0]$  take place, and finally, the full system is transformed by 2 377 335 MCS. (d) Time dependence of P and T populations and electrical conductivity through the SAM during T-to-P transition.

conditions. Our code employed the Metropolis algorithm, with each Monte Carlo step (MCS) defined as  $50 \times 50 = 2500$  MC trials with a fixed external field applied in the  $[0001]$  direction. These MC simulations are similar to the previous study of an Ising model in a time-dependent magnetic field, which was applied to investigate the magnetic hysteresis loop.<sup>32</sup>

We simulated the response of the SAM initially covered with all P's to the  $1.2 \text{ V}/\text{\AA}$  external field during  $1.2 \times 10^6$  Monte Carlo steps (MCS) at  $T = 300 \text{ K}$ . Figures 6a and 6b show the time evolution of the system starting with all P's and ending with all T's and the population change with the electrical conductivity change during this P-to-T transition, respectively. In our simulations, we observed no T states until just before 55 184 MCS, but within the next 15 steps, half of the neighbors along  $[1\bar{1}\bar{2}0]$  have transformed, and after another 15 steps the entire  $[1\bar{1}\bar{2}0]$  line is transformed to the T. Then, by 405 907 MCS a total of 19  $[1\bar{1}\bar{2}0]$  lines have transformed, all of which are neighbors to the original transformed line. Then, at 486 389 MCS, we see that a second  $[1\bar{1}\bar{2}0]$  swath has nucleated. By 697 272 MCS, these two have grown to 28 and 7 adjacent lines but still just two swathes. Then, from 697 273 MCS, they are merged into one swathe. Finally, by 1 008 706 MCS, the full system is transformed to T. The electrical conductivity of the entire SAM is evaluated from the

convolution of a fraction of each conformation (Figure 6b) with its characteristic  $I-V$  curve (Figure 4). Along with the decrease of the P population, the total conductivity through the SAM also decreases.

The analysis of the snapshots demonstrates that the time to complete the transformation of each line in  $[1\bar{1}\bar{2}0]$  after initiation is 26.32 MCS, leading to the rate constant of propagation  $k_{[1\bar{1}\bar{2}0]} = 5.48 \text{ \AA}/\text{MCS}$ . The  $k_{[1\bar{1}\bar{2}0]}$  shows almost no dependence on the temperature (Figure 7a, top), which suggestss that the energy barrier for the propagation is negligible. Thus, once one AN-OPE is switched, it nucleates the transformation which propagates quickly along the  $[1\bar{1}\bar{2}0]$  line. This is quite reasonable, given the energetic stability of  $\text{P}_2\text{T}_2_{[1\bar{1}\bar{2}0]}$  (Figure 5). Later, another nucleation event occurs leading to subsequent transformation of another  $[1\bar{1}\bar{2}0]$  line. Typically this subsequent transformation takes place adjacent to the precedent transformed line in the  $[1\bar{1}00]$  direction.

Therefore, the rate-determining step for the entire phase transition is nucleation, as usual, nucleation-propagation mechanisms. The middle panel of Figure 7a shows the probability,  $P(t)$ , of exhibiting no nucleation until time  $t$ . To obtain the nucleation time ( $\tau$ ) when one  $[1\bar{1}\bar{2}0]$  line is already transformed, we analyzed the nucleation events initiated next to the  $[1\bar{1}\bar{2}0]$

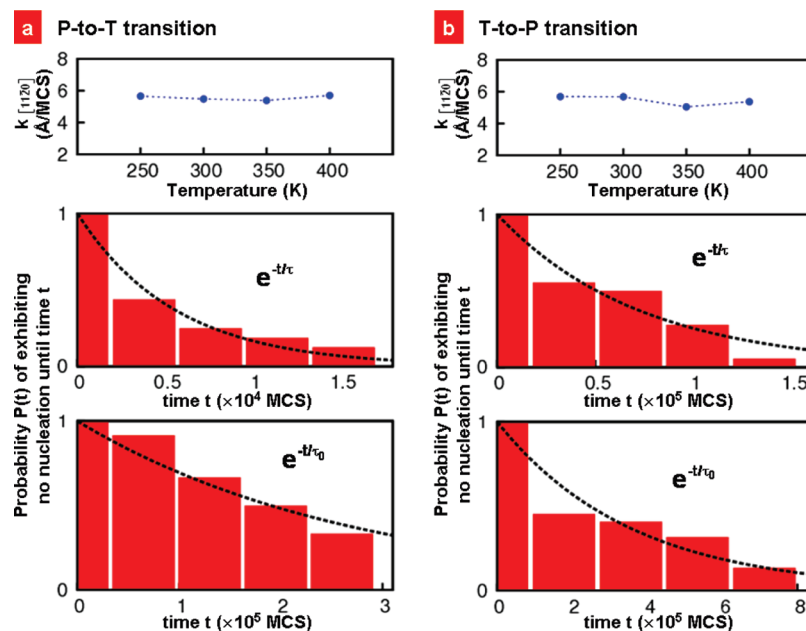


**Figure 7.** (a) P-to-T transition; (b) T-to-P transition. Top panels show the temperature dependence of the propagation rate along  $[11\bar{2}0]$ ,  $k_{[11\bar{2}0]}$ . Middle panels show the probability,  $P(t)$ , of exhibiting no nucleation by time  $t$  for the case when the nucleation is initiated next to another  $[11\bar{2}0]$  line. The dotted lines is an exponential fit of  $P(t)$ . This leads to a nucleation rate of  $\tau = 5583$  MCS for the P-to-T transition and  $\tau = 72\,926$  MCS for the T-to-P transition. Bottom panels show the probability,  $P(t)$ , of exhibiting no nucleation by time  $t$  for the case when the nucleation is initiated in the absence of the next  $[11\bar{2}0]$  line. The exponential fit leads to a nucleation rate of  $\tau_0 = 274\,193$  MCS for the P-to-T transition and  $\tau_0 = 357\,135$  MCS for the T-to-P transition.

line among the snapshots. We found that the nucleation process is a Poisson process, in which  $P(t)$  decays exponentially with time. We obtained a value of  $\tau = 5583$  MCS by fitting  $P(t)$ .

To obtain the nucleation time ( $\tau_0$ ) in the absence of the transformed  $[11\bar{2}0]$  line, we carried out an additional 50 simulations to determine when the first P transforms to the T, showing that this process proceeds as a Poisson process with  $\tau_0 = 274\,193$  MCS, which is  $\sim 50$  time larger than  $\tau$ . (See the bottom panel of Figure 7a.)

Figures 6c shows the time evolution of the system with no external field starting with all T's and ending with all P's, while Figure 6d shows the population change with the electrical conductivity change during this T-to-P transition. The overall process is quite similar to that of the P-to-T transition. The first nucleation occurred at 486 389 MCS, and then, the neighbors along  $[11\bar{2}0]$  showed fast transition to P within 21 MCS. While this swath is growing along the  $[1\bar{1}00]$  direction, the second and the third nucleation without next transformed line occurred at 1 174 624 MCS and 1 239 313 MCS, respectively. Finally, the full system is transformed to P by 2 377 335 MCS. During the transition, the total conductivity through the SAM increases along with the decrease of the P population.

During T-to-P transition, the average time to complete each line of  $[11\bar{2}0]$  growth is 25.38 MCS, leading to  $k_{[11\bar{2}0]} = 5.68$  Å/MCS with no temperature dependency (Figure 7b, top panel).

The nucleation times were studied in the same manner as the P-to-T transition. The nucleation process follows Poisson statistics with  $\tau = 72\,926$  MCS and  $\tau_0 = 357\,135$  MCS in the presence and the absence of the next transformed  $[11\bar{2}0]$  line, respectively (Figure 7b, middle and bottom panels).

The interaction between P and T is smaller than the interaction between P and P or T and T by an average of  $\sim 8.6$  kcal/mol (Table 1), due to the loss of HB or less-favorable van der Waal's

interaction caused by the packing of two different conformations. This infers that the boundary of  $[11\bar{2}0]$  line is energetically less stable, leading to a fast transformation at the boundary. This well explains why  $\tau$  is smaller than  $\tau_0$ .

We also found  $\tau$  during the P-to-T transition is smaller than  $\tau$  during the T-to-P transition. This is because the formation of the T-T HB network is accompanied by the expansion of the  $[11\bar{2}0]$  swath along  $[1\bar{1}00]$  during the P-to-T transition, while the loss of the T-T HB network is accompanied during the T-to-P transition.

**NDR for Time-Dependent Electric Field.** Applying a time-dependent external field, we calculated the response of the system to voltage sweeps at various sweep rates. For each sweep, the magnitude of the external field was increased linearly until  $F = 1.4$  V/Å (corresponding to 1.5 V bias voltage in the forward sweep; see Appendix S1 of the Supporting Information), and then it was decreased at the same rate until the field was 0 V/Å (corresponding to 0 V bias voltage in backward sweep). The sweep rates were  $1 \times 10^{-8}$ ,  $4 \times 10^{-8}$ , and  $2 \times 10^{-7}$  V/MCS.

The resultant  $I-V$  curves are shown in Figure 8a. Although the current drops dramatically at sufficiently high voltage for all cases, we found that faster sweeps let the systems stay in the P phase at higher voltage, which agrees with experimental observations. Thus, the simulations show clearly both the NDR phenomena and the hysteretic behavior with sweep rate dependence as observed experimentally. During the backward sweep, the simulations find that the T state transforms back to P at  $\sim 0.2$  V bias voltage with slower sweep rates.

To determine the total charge associated with the NDR region, we integrated the current from the peak to the valley in Figure 8a. This amount of charge ( $Q_F$ ) flowing through the junction during NDR is an important physical quantity that characterizes the QC model.<sup>5</sup> The calculated  $Q_F$  values are

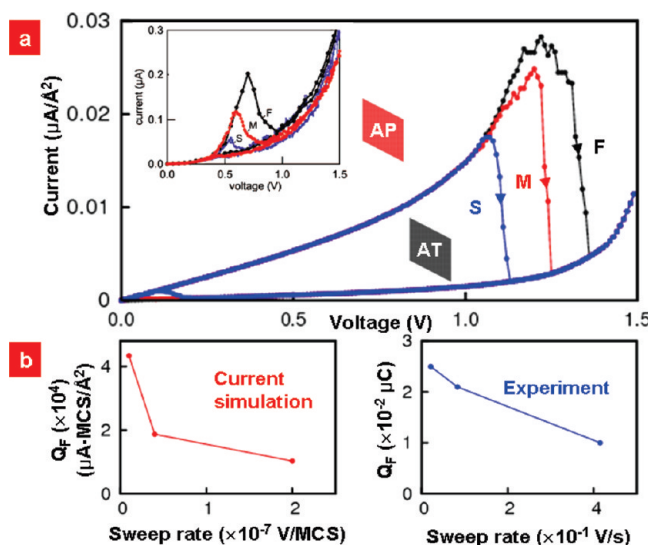


**Figure 8.** (a) Current–voltage ( $I$ – $V$ ) curves calculated at 300 K from MC simulations combined with the  $I$ – $V$  results of the QM Green's function calculations. Results for three sweeping rates are shown: S (blue line),  $1 \times 10^{-8}$  V/MCS; M (red line),  $4 \times 10^{-8}$  V/MCS; F (black line),  $2 \times 10^{-7}$  V/MCS. Inset is the experimental  $I$ – $V$  curves from the ref 4 with three different sweeping rates: S (blue line), 21 mV/s; M (red line), 83 mV/s; F (black line), 415 mV/s. (b) Sweep rate dependence of the integral of the current from the peak to the valley during NDR,  $Q_F$ , from current simulation (left panel) and experiment<sup>4</sup> (right panel).

- $Q_F = 4.34 \times 10^4 \mu\text{A}\cdot\text{MCS}/\text{Å}^2$  for sweep rates of  $1 \times 10^{-8}$  V/MCS
- $Q_F = 1.87 \times 10^4 \mu\text{A}\cdot\text{MCS}/\text{Å}^2$  for sweep rates of  $4 \times 10^{-8}$  V/MCS, and
- $Q_F = 1.03 \times 10^4 \mu\text{A}\cdot\text{MCS}/\text{Å}^2$  for sweep rates of  $2 \times 10^{-7}$  V/MCS.

Figure 8b shows the sweep rate versus  $Q_F$  plots from the simulation (left panel) and from the experiment (right panel). The simulations reproduce the experimental observation that  $Q_F$  decreases with increasing sweep rate. Additionally, we find that changing the sweep rate by 20 times only changes the  $Q_F$  by 4.2 times, which can be compared to the experimental observation that the  $Q_F$  varies 2.5 times while the sweep rate changes by  $\sim 20$  times.<sup>5</sup>

The NDR peak from the MC simulations is sharp over a voltage range of  $\sim 0.15$  V while the experimental NDR peak is smooth with a range of  $\sim 0.25$  V. The sharpness and smaller voltage range in the simulations may result from the finite size of the simulation cell with the use of periodic boundary conditions (PBC). The size of our periodic cell is  $1620 \text{ nm}^2$  compared to the experiment of  $0(\text{cm}^2)$ . To check the finite size effect of the PBC, we obtained the total time taken for the complete P-to-T transition under the constant external field of  $F$ ,  $t_{\text{P-to-T}}(F)$ , for various PBC cell sizes of  $10 \times 10 = 100$ ,  $30 \times 30 = 900$ ,  $40 \times 40 = 1600$ ,  $50 \times 50 = 2500$ , and  $60 \times 60 = 3600$ . The dependence of  $t_{\text{P-to-T}}(F)$  on the cell dimension is shown in Figure 9. We found that the finite size effect highly overestimated the  $t_{\text{P-to-T}}(F)$ , and this tendency is maximized when the external electric field is near the critical point of  $F_c$  ( $=0.56 \text{ V}/\text{\AA}$ ) where phase transition occurs. It is well-known that this finite-size effect becomes serious near the critical point of a phase transition.<sup>18</sup> As a result, the system does not show the phase transition for moderate external fields; instead, it eventually occurs in a rapid and simultaneous

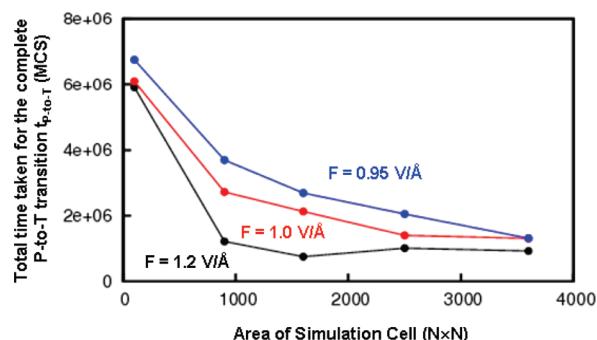


**Figure 9.** Total time taken for the complete P-to-T transition,  $t_{\text{P-to-T}}$ , by varying the area of the periodic simulation cell as  $10 \times 10 = 100$ ,  $30 \times 30 = 900$ ,  $40 \times 40 = 1600$ ,  $50 \times 50 = 2500$ , and  $60 \times 60 = 3600$ . The black line denotes the change of  $t_{\text{P-to-T}}$  under the external field of  $F = 1.2 \text{ V}/\text{\AA}$ , the red line denotes the change of  $t_{\text{P-to-T}}$  scaled by 10 under the external field of  $F = 1.0 \text{ V}/\text{\AA}$ , and the blue line denotes the change of  $t_{\text{P-to-T}}$  scaled by 15 under the external field of  $F = 0.95 \text{ V}/\text{\AA}$ . The  $t_{\text{P-to-T}}$  value is converged at the areas of  $900$ – $1600$  and  $2500$ – $3600$  when  $F = 1.2$  and  $1.0 \text{ V}/\text{\AA}$ , respectively. When  $F = 0.95 \text{ V}/\text{\AA}$ , the  $t_{\text{P-to-T}}$  value is not converged until the area of  $3600$ . This infers that we need much larger simulation cell to get the right converged value of  $t_{\text{P-to-T}}$  as  $F$  approaches the critical field,  $F_c = 0.56 \text{ V}/\text{\AA}$ . Otherwise, we will get the overestimated value of  $t_{\text{P-to-T}}$  near  $F_c$ .

manner at very high electric fields. This leads the theoretical NDR to be sharp and narrow.

We also idealized the degrees of freedom for the molecules into two states, which consider the perfectly crystallized phases for infinite AN-OPEs to be connected through the HB network. In an actual device, many other states are possible that differ only by slight changes in the orientation of the AN-OPE since it is a flexible molecule. This flexibility of the SAM at 300 K will broaden the energy density of states of P and T, making the phase transition become smoother. Furthermore, we can consider the possibility of formation of disordered states, i.e., noncrystalline phases during the kinetic process of voltage sweep. Once some part of the AN-OPE SAM is disordered, it will not be responsible for the NDR behavior. We believe the experimental observation that the NDR peak decreasing with successive sweep cycles and eventually disappearing<sup>34</sup> is caused by the expansion of disordered phases.

Next, we examined if our mechanism for AN-OPE can account for the NDR behaviors of other OPE-derivative systems. The bare OPE (B-OPE) containing no  $\text{NH}_2$  or  $\text{NO}_2$  group can have neither a significant dipole moment nor HB network. Therefore, no NDR peak is expected for B-OPE SAM systems, in agreement with experiment.<sup>34</sup> For the 2-nitro-OPE (N-OPE) SAM containing only  $\text{NO}_2$  group without  $\text{NH}_2$  group, we found that it can form a similar HB network (see Figure 10, and details are described in Appendix S2 of the Supporting Information). This infers that the N-OPE SAM system can show a similar NDR behavior, also in agreement with experiment.<sup>34</sup>

## CONCLUSIONS

We suggest a mechanism to explain the room temperature hysteretic NDR behavior observed in Kiehl's metal–molecule–metal junctions. Using a multiscale simulation paradigm, we developed a coarse-grained nearest neighbor interaction Hamiltonian from the energetics determined by first-principles methods. By coupling the coarse-grained Hamiltonian with the Monte Carlo technique, we were able to explain the origin of the hysteretic NDR.

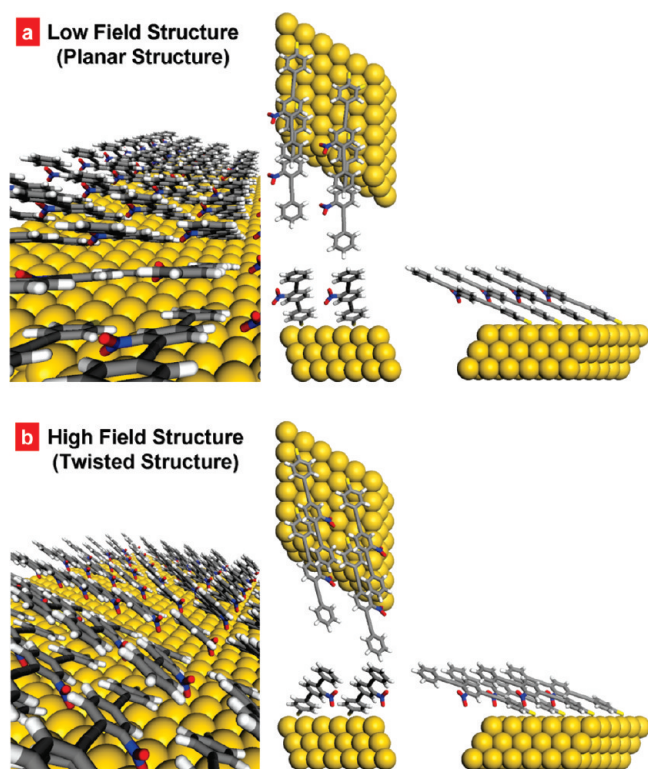


**Figure 10.** (a) Optimized geometry for the low-field structure (P) of N-OPE SAM. Here [0001] is the surface normal, and the views are along the z-axis (upper middle), y-axis (lower middle), and x-axis (lower right). The left picture is a perspective along the axis of one plane of molecules. The weak hydrogen bonding network is aligned along the  $[1\bar{1}\bar{2}0]$  direction. (b) Optimized geometry for the high-field structure (T) of N-OPE SAM. Here [0001] is the surface normal, and the views are along the z-axis (upper middle), y-axis (lower middle), and x-axis (lower right). The left picture is a perspective along the axis of one plane of molecules. The weak hydrogen bonding network is aligned along the  $[1\bar{1}\bar{2}0]$  direction.

According to our mechanism, experimentally observed NDR behavior is the consequence of the kinetic effect of the molecular AN-OPE SAM during the voltage sweep cycle. The energetic preference between two different phases (named as P and T) is altered by the balance of intermolecular interactions (two-body interaction term) and the dipole–electric field interaction (one-body interaction term). The P phase has better intermolecular interactions making it stable in low bias-voltage, while the T phase has a better dipole–electric field interaction due to the rotation of the second phenyl ring, which stabilizes it at high bias-voltage. Thus, the forward voltage sweep induces the rotation of the second phenyl ring of the AN-OPE molecules, leading a P-to-T phase transition while backward voltage sweep induces the T-to-P phase transition. This rotation of the second phenyl ring suppresses the  $\pi$  orbital overlaps between phenyl rings, which result in the lower electrical conductance of the T phase compared to the P phase.

We investigated the kinetics during the electric-field-induced phase transitions using Monte Carlo simulation techniques, leading to qualitative agreement with experiments covering observances in other OPE-derivative-based devices. Our results provide a plausible mechanism for understanding the observed room-temperature NDR phenomena which should be useful in developing molecular systems exhibiting the type of NDR characteristics needed for practical electronic circuitry.

## ASSOCIATED CONTENT

**S Supporting Information.** Appendices A1 and A2 and Figures S1–S3. This material is available free of charge via the Internet at <http://pubs.acs.org>.

## AUTHOR INFORMATION

### Corresponding Author

\*E-mail wag@wag.caltech.edu.

## ACKNOWLEDGMENT

The computational work was initiated with support by the National Science Foundation (NIRT, W.A.G.). The collaboration was supported by the Microelectronics Advanced Research Corporation (MARCO, W.A.G. and R.A.K.) and its Focus Centers on Functional Engineered NanoArchitectonics (FENA). The facilities of the MSC (W.A.G.) were supported by ONR-DURIP, ARO–DURIP, and the facilities of the CNBT lab (S.S.J.) were supported by the startup from the MSE in Georgia Tech. H.K. and W.A.G. acknowledge support from the WCU (World Class University) program through the National Research Foundation of Korea funded by the Ministry of Education, Science and Technology (R31-2008-000-10055-0).

## REFERENCES

- (1) Esaki, L. *Phys. Rev.* **1958**, *109*, 603.
- (2) Xue, Y. Q.; Datta, S.; Hong, S.; Reifenberger, R.; Henderson, J. I.; Kubiak, C. P. *Phys. Rev. B* **1999**, *59*, R7852.
- (3) Selzer, Y.; Salomon, A.; Ghabboun, J.; Cahen, D. *Angew. Chem., Int. Ed.* **2002**, *41*, 827.
- (4) Pitters, J. L.; Wolkow, R. A. *Nano Lett.* **2006**, *6*, 390.
- (5) Kiehl, R. A.; Le, J. D.; Candra, P.; Hoye, R. C.; Hoye, T. R. *Appl. Phys. Lett.* **2006**, *88*.
- (6) Tao, N. J. *Nat. Nanotechnol.* **2006**, *1*, 173.
- (7) Chen, J.; Reed, M. A.; Rawlett, A. M.; Tour, J. M. *Science* **1999**, *286*, 1550.
- (8) Guisinger, N. P.; Yoder, N. L.; Hersam, M. C. *Proc. Natl. Acad. Sci. U.S.A.* **2005**, *102*, 8838.
- (9) He, J.; Lindsay, S. M. *J. Am. Chem. Soc.* **2005**, *127*, 11932.
- (10) Salomon, A.; Arad-Yellin, R.; Shanzer, A.; Karton, A.; Cahen, D. *J. Am. Chem. Soc.* **2004**, *126*, 11648.
- (11) Kratochvilova, I.; Kocirik, M.; Zambova, A.; Mbindyo, J.; Mallouk, T. E.; Mayer, T. S. *J. Mater. Chem.* **2002**, *12*, 2927.
- (12) Rawlett, A. M.; Hopson, T. J.; Nagahara, L. A.; Tsui, R. K.; Ramachandran, G. K.; Lindsay, S. M. *Appl. Phys. Lett.* **2002**, *81*, 3043.
- (13) Amlani, I.; Rawlett, A. M.; Nagahara, L. A.; Tsui, R. K. *Appl. Phys. Lett.* **2002**, *80*, 2761.
- (14) Donhauser, Z. J.; Mantooth, B. A.; Kelly, K. F.; Bumm, L. A.; Monnell, J. D.; Stapleton, J. J.; Price, D. W.; Rawlett, A. M.; Allara, D. L.; Tour, J. M.; Weiss, P. S. *Science* **2001**, *292*, 2303.
- (15) Fan, F. R. F.; Lai, R. Y.; Cornil, J.; Karzazi, Y.; Bredas, J. L.; Cai, L. T.; Cheng, L.; Yao, Y. X.; Price, D. W.; Dirk, S. M.; Tour, J. M.; Bard, A. J. *J. Am. Chem. Soc.* **2004**, *126*, 2568.
- (16) Seminario, J. M.; Zacarias, A. G.; Tour, J. M. *J. Am. Chem. Soc.* **2000**, *122*, 3015.
- (17) Xiao, X. Y.; Nagahara, L. A.; Rawlett, A. M.; Tao, N. J. *J. Am. Chem. Soc.* **2005**, *127*, 9235.
- (18) Reed, M. A.; Chen, J.; Rawlett, A. M.; Price, D. W.; Tour, J. M. *Appl. Phys. Lett.* **2001**, *78*, 3735.
- (19) Chen, J.; Wang, W.; Reed, M. A.; Rawlett, A. M.; Price, D. W.; Tour, J. M. *Appl. Phys. Lett.* **2000**, *77*, 1224.
- (20) Sollner, T. C. L. G.; Goodhue, W. D.; Tannenwald, P. E.; Parker, C. D.; Peck, D. D. *Appl. Phys. Lett.* **1983**, *43*, 588.

- (21) Tsuchiya, M.; Sakaki, H.; Yoshino, J. *Jap. J. Appl. Phys., Part 2: Lett.* **1985**, *24*, L466.
- (22) Qiu, X. H.; Nazin, G. V.; Ho, W. *Phys. Rev. Lett.* **2004**, *93*, 4.
- (23) Akdim, B.; Pachter, R. *J. Phys. Chem. C* **2008**, *112*, 3170.
- (24) Troisi, A.; Ratner, M. A. *Nano Lett.* **2004**, *4*, 591.
- (25) Emberly, E. G.; Kirczenow, G. *Phys. Rev. B* **2001**, *64* 12.
- (26) Galperin, M.; Ratner, M. A.; Nitzan, A. *Nano Lett.* **2005**, *5*, 125.
- (27) Kresse, G.; Furthmuller, J. *Phys. Rev. B* **1996**, *54*, 11169.
- (28) Jaguar package, V. 6.5 ed.; Schroedinger Inc.: Portland, OR, 2005.
- (29) Schultz, P. SeqQuest program; Sandia National Laboratories: Albuquerque, NM, 2003.
- (30) Kim, Y. H.; Jang, S. S.; Jang, Y. H.; Goddard, W. A. *Phys. Rev. Lett.* **2005**, *94*.
- (31) Mayo, S. L.; Olafson, B. D.; Goddard, W. A. *J. Phys. Chem.* **1990**, *94*, 8897.
- (32) Lo, W. S.; Pelcovits, R. A. *Phys. Rev. A* **1990**, *42*, 7471.
- (33) Stokbro, K.; Taylor, J.; Brandbyge, M.; Ordejon, P. *Mol. Electron. Iii* **2003**, *1006*, 212.
- (34) Candra, P. University of Minnesota, 2006.